MRI data acquisition

The two imaging facilities are an outpatient imaging facility and a regional hospital that routinely perform breast MRI but have different service contracts and quality control guidelines. Note again that the repeatability and reproducibility of quantitative MRI at these centers was previously established [1, 2]. Breast MRI employed Siemens 3T scanners (Erlangen, Germany) equipped with an 8- or 16-channel receive double-breast coil (Sentinelle, Invivo, Gainesville, Florida). All images were acquired in the sagittal plane. Diffusion-weighted MRI (DW-MRI) was acquired using a monopolar, single-shot spin echo, echo planar imaging sequence in a diagonal diffusion-encoding direction. Six acquisitions were averaged for *b*-values of 0 and 200 s/mm^2, while 18 acquisitions were averaged for a *b*-value of 800 s/mm^2. (This allowed for approximately equal signal-to-noise ratios at all *b*-values.) DW-MRI was acquired over 10 slices with 5 mm thickness and no slice gap. Spectrally selective adiabatic inversion recovery (SPAIR) fat suppression was included for a total scan time of 1 minute 39 seconds. Additional acquisition parameters were repetition time/echo time (*TR/TE)* = 3000/52 ms, flip angle 90°, matrix = 128 × 128 (over a 256 × 256 mm^2 field-of-view), and a GeneRalized Autocalibrating Partial Parallel Acquisition (GRAPPA) acceleration of 2.

The MRI protocol also included a high-resolution T_1- weighted, 3D gradient-echo, FLASH (fast low angle shot) acquisition using the following parameters: *TR*/*TE* = 5.3/2.3 milliseconds, flip angle = 10°, acquisition matrix = 256 × 256, slice thickness = 1 mm, GRAPPA acceleration of 2, and SPAIR (Spectral Selection Attenuated Inversion Recovery) fat suppression. Acquisition time for the anatomical image was 3 minutes and 11 seconds. The DCE-MRI protocol consisted of a T_1-weighted, VIBE (Volumetric Interpolated Breath-hold Examination; though no breath-holding was employed in these studies) acquisition with *TR*/*TE* = 7.02/4.6 ms, a flip angle of 6°, matrix = 192 × 192, with 10 slices of 5 mm thickness each, and a GRAPPA acceleration factor of 3 yielding a temporal resolution of 7.27 seconds for 1 minute prior to and 6 minutes post administration of a gadolinium-based contrast agent (Multihance (Bracco, Monroe Township, NJ) or Gadovist (Bayer, Leverkusen, Germany)) *via* a power injector followed by a saline flush. A Siemens TurboFLASH sequence was used to map the B_1 field to correct for transmit inhomogeneity with the following acquisition parameters: *TR*/*TE* = 8680/2 milliseconds, flip angle = 8°, matrix = 96 × 96, and slice thickness = 5 mm. Due to the inclusion of a slice gap in the B_1 mapping protocol, two acquisitions were performed to cover the same field-of-view as the above

measurements for a total acquisition time of 34 seconds. See Taable S.1 for a summary of all imaging parameters.

Table S.1 Breast MRI acquisition parameters. All breast MRI data were acquired in the sagittal plane with a field of view of 256 × 256 mm. For the DW-MRI, six acquisitions were averaged for *b*-values of 0 and 200 s/mm^2, while 18 acquisitions were averaged for a *b*-value of 800 s/mm^2. DCE-MRI data had a temporal resolution of 7.27 seconds.

MRI parameters	DW-MRI	B_1 mapping*	T_1 mapping: variable flip angle	DCE-MRI
Scan sequence	single-shot spin echo, echo planar	TurboFLASH	3D gradient-echo FLASH	T_1-weighted, VIBE
TR (ms)	3000	8680	5.3	7.02
TE (ms)	52	2	2.3	4.6
Flip angle (degrees)	90	8	20	6
Acquisition matrix	128×128	96×96	256×256	192×192
Slice thickness	5	5	1	5
GRAPPA acceleration factor	2	N/A	2	3
Fat suppression	SPAIR	SPAIR	SPAIR	N/A

*Due to the inclusion of a slice gap in the B_1 mapping protocol, two acquisitions (at 17 seconds each) were performed to cover the same field-of-view as the other measurements.

Data analysis techniques

See Figure S.1 for a summary of all the data analysis and processing steps. Two types of image registrations were performed on each data set: intra-scan (registration within a single visit) and inter-scan (registration across visits). For each patient, the MR images acquired at each session (intra-scan) were aligned using a rigid registration algorithm where the B_1, T_1, and diffusion-weighted images were registered to the DCE images. Images acquired at a different resolution compared to the DCE images were upsampled using a nearest neighbor approach *via* MATLAB's (MathWorks, Natick, MA) function *interp3.* The rigid algorithm used for the intra-scan registration was implemented using MATLAB's function *imregister*. For each patient, all image data sets were registered across time (inter-scan) to a common space *via* a non-rigid registration algorithm with a constraint that preserves the tumor volumes at each time point [3]. The inter-scan registration employs an adaptive basis algorithm performed using the software Elastix [4, 5].

The DCE-MRI data were used for both tissue segmentation and characterizing the vasculature for each patient. The DCE-MRI data were used to segment the tumor region of interest (ROI) at each time point using a fuzzy c-means-based clustering algorithm [6]. The clustering algorithm partitions the voxels into classes based on a probability weighting for likely voxel membership to the tumor ROI. To generate masks of fibroglandular and adipose tissues, MATLAB's *adapthisteq* function was first applied to enhance the post inter-scan registered DCE images, which uses a contrast-limited adaptive histogram equalization algorithm. The fibroglandular and adipose tissues were segmented using a *k*-means clustering algorithm (these masks are used for the assignment of tissue stiffness properties in the mathematical model detailed below).

The DCE-MRI data were analyzed using the standard Kety-Tofts model:

$$C_t(\bar{x},t) = K^{trans}(\bar{x}) \int_0^t \left(C_p(u) \cdot \exp\left(-\frac{K^{trans}(\bar{x})}{v_e(\bar{x})} (t-u) \right) \right) du, \qquad \text{(S1)}$$

where $C_t(\bar{x},t)$ and $C_p(t)$ are the concentrations of the contrast agent in the tissue and plasma at position $\bar{x}$ and time t, respectively; $K^{trans}(\bar{x})$ is the volume transfer constant from the plasma space to the tissue space at position x, and $v_e(\bar{x})$ is the volume fraction of the extravascular extracellular space at position x. (For more details on this model, see [7].) Eq. (S.1) was fit to the DCE-MRI data from each voxel within the tumor using a population averaged $C_{plasma}(t)$ that was established

from the present data set according to the method developed in [8]. Voxels for which Eq. (S.1) did not converge or converged to non-physical values (i.e., K^{trans}, $v_e < 0$, or $v_e > 1$) were removed.

To approximate the drug distribution in each voxel of tissue, a normalized map of the blood volume is calculated by computing the area under the dynamic curve (AUC) of the baseline-subtracted time course for each voxel, and then normalizing by the maximum AUC value from the whole tumor ROI. This normalized blood volume map is then scaled by the peak concentration of drug (as estimated from the Kety-Tofts model [9]) to define the initial drug distribution throughout the domain at the time of each dose of therapy. Specifically, the Kety-Tofts model (i.e., Eq. (S1)) and the DCE-MRI derived physiological parameters per voxel are used where the concentration of contrast agent in the plasma is replaced with the concentration of drug in the plasma from measured population curves for each therapy [10-13]. Therefore, the concentration of drug in the tumor tissue is spatially non-uniform and temporally varying based on the individual patient's NAT schedule and vascular characteristics [9].

The apparent diffusion coefficient (*ADC*) values for individual voxels were calculated using the DW-MRI data *via* standard methods [14]. Then the *ADC* value for each voxel within the tumor (as segmented using the above methods) was converted to an estimate for the number of tumor cells per voxel at each 3D position $\bar{x}$ and time t, $N_{TC}(\bar{x},t)$, *via* our established methods [9, 14-17]:

$$N_{TC}(\bar{x},t) = \theta\left(\frac{ADC_w - ADC(\bar{x},t)}{ADC_w - ADC_{min}}\right), \tag{S2}$$

where ADC_w is the *ADC* of free water (3×10^{-3}mm^2/s) [18], $ADC(\bar{x},t)$ is the *ADC* value for the voxel at position x and time t, and ADC_{min} is the minimum *ADC* value over all tumor voxels for the patient [19, 20]. The parameter θ is the carrying capacity describing the maximum number of tumor cells that can physically fit within a voxel; its numerical value is determined by assuming a spherical packing density of 0.7405 [21], a nominal tumor cell radius of 10 μm, and the voxel volume (8.45 mm^3).

The tumor volume was approximated as the product of the total number of voxels within the segmented tumor ROI and the DCE-MRI voxel volume. To calculate the longest axis of each tumor, the 3D tumor ROI was evaluated by MATLAB's *regionprops3* function, which approximates the longest possible axis within a 3D object. These measures of tumor volume and longest axis are also applied to all the model's predictions (where the model uses the same domain as the MR images) for direct comparison to the experimentally measured values.

Figure S.1: The MRI data goes through four different steps prior to incorporation into the mathematical model: intra-scan registration, data processing, inter-scan registration, and calculation of the modeling quantities. While more details can be found in the above text and in the figure, briefly, inter-scan registration consists of the alignment of the different MRI data types (panels a and b) within each scan session to correct for any possible motion that occurred during the scan visit. The data processing step consists of deriving values from each of the MRI data sets to identify the region of interest (panel c), quantify the vasculature (panel d), and define values to determine cellular density of the tumors (panel e). The inter-scan registration consists of aligning all of the MRI scans for each patient across time (panel f). The final step consists of taking the registered data and defining the specific quantities to be used in the mathematical model including the breast region for modeling (panel g), tissue maps (panel h), tumor cell numbers (panel i), and drug concentrations (panel j).

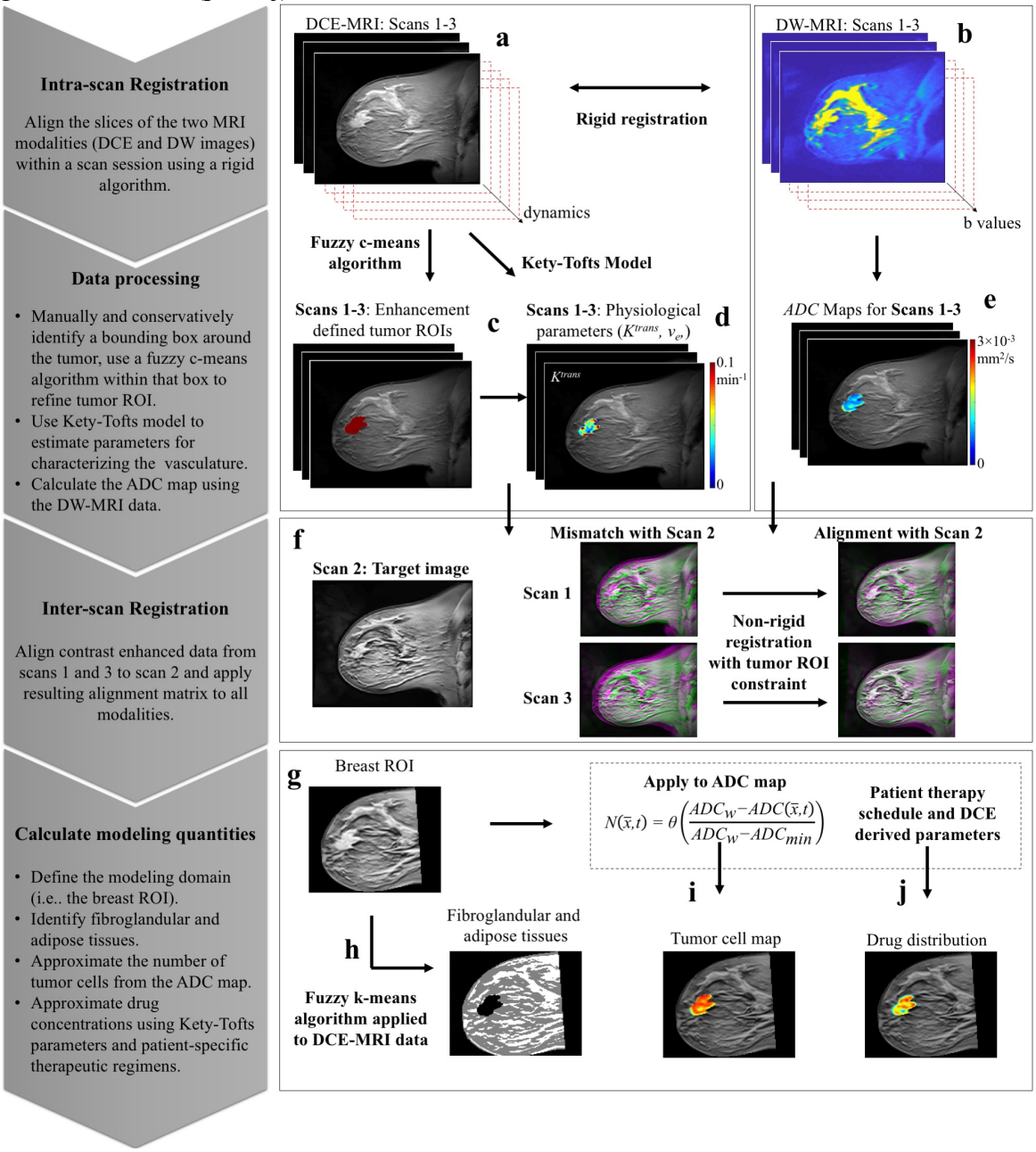

Mathematical Model

To improve readability, we restate (from the main text) the model equations and descriptions. We have previously developed a 3D mathematical model that includes the mechanical coupling of tissue properties to tumor growth and the delivery of therapy [9]. This model was designed to be initialized with patient-specific, quantitative, MRI data for breast cancer to predict therapy response. The current work extends this previous approach to account for multiple chemotherapy terms. The governing equation for the spatiotemporal evolution of tumor cells, $N_{TC}(\bar{x},t)$, is:

$$\frac{\partial N_{TC}(\bar{x},t)}{\partial t} = \overbrace{\nabla\cdot(D(\bar{x},t)\nabla N_{TC}(\bar{x},t))}^{\text{diffusion}} + \overbrace{k(\bar{x})(1- N_{TC}(\bar{x},t)/\theta(\bar{x}))N_{TC}(\bar{x},t)}^{\text{growth}} - \overbrace{C_{drug}(\bar{x},t)N_{TC}(\bar{x},t)}^{\text{therapy}}, \quad \text{(S3)}$$

where the first term on the right-hand side describes tumor cell movement, the second term describes the logistic growth of the cells, and the third term describes the effect of chemotherapy. (See Tables S.1 and S.2 for descriptions of the variables and parameters, as well as how they are assigned.) For the growth term, $k(\bar{x})$ is a spatially resolved proliferation rate map for tumor cells, and the parameter θ is the carrying capacity for logistic growth and is defined as in the previous supplemental section, while the proliferation rate is calibrated per voxel for each individual patient. The first term of Eq. (S3), representing the random diffusion (movement) of the tumor cells, $D(\bar{x},t)$, is mechanically linked to the breast tissue's material properties *via*:

$$D(\bar{x},t) = D_0\exp(-\gamma\sigma_{vm}(\bar{x},t)), \quad \text{(S4)}$$

where $D(\bar{x},t)$ is the diffusion coefficient, D_0 the tumor cell diffusion constant in the absence of stress (please note that D_0 is the diffusion value for the tumor cells and is not to be confused with the *ADC*, which is the apparent diffusion coefficient of water molecules), γ an empirical coupling constant for the von Mises stress, σ_{vm}. The von Mises stress reflects the total stress experienced for a given section of tissue; while it is often used as failure criterion in material testing, here it is used to reflect the interaction between the growing tumor and its environment. Therefore, when there is no stress, the diffusion coefficient is equal to D_0. Additionally, a linear elastic, isotropic equilibrium between the tumor and its environment dependent upon changes in tumor cell number is enforced through:

$$\nabla\cdot G\nabla\vec{u} + \nabla\frac{G}{1 - 2\nu}(\nabla\cdot\vec{u}) - \lambda\nabla N_{TC}(\bar{x},t) = 0, \quad \text{(S5)}$$

where G = $E/(2(1 - \nu))$ is the shear modulus with Young's modulus (E) and Poisson's ratio (ν) material properties, $\vec{u}$ is the displacement due to tumor cell growth, and λ is another empirical coupling constant [15, 16, 22-28]. Briefly, this model describes tumor growth changes that can cause deformations in the surrounding healthy tissues (breast fibroglandular tissue and adipose tissue), potentially increasing stress and therefore reducing the outward expansion of the tumor.

The therapy term in Eq. (S3) describes the spatiotemporal distribution of each drug in the tissue and its effect on the cells of each voxel. Here we have expanded the model (from previous efforts [9]) to acknowledge their differing efficacies and decay rates using the following equation:

$$C_{drug}(\bar{x},t) = \overbrace{\alpha_1 C_{drug_1}(\bar{x},t^*)\exp(-\beta_1 t)}^{\text{chemotherapy 1}} + \overbrace{\alpha_2 C_{drug_2}(\bar{x},t^*)\exp(-\beta_2 t)}^{\text{chemotherapy 2}}, \quad \text{(S6)}$$

where α_i is the efficacy of the i^{th} drug on the tumor cells, $C_{drug_i}(\bar{x},t^*)$ is the initial concentration of each drug for each dose with the variable t^* being time relative to the patient scan data (described in more detail below), and the exponential decay terms, $\exp(-\beta_i t)$, represent the eventual washout of the drug over time after each dose. The α_i and β_i parameters are calibrated for each patient and each drug, where the β_i calibration is restricted using bounds defined from ranges found in the literature for the terminal half-lives of each drug [29-34]. The initial concentration of drug, $C_{drug_i}(\bar{x},t^*)$, is approximated using the DCE-MRI data as described in the previous section. This concentration is dependent on the time t^*, indicating that for the calibration of the model the drug distribution map may be derived from scan 1, but an updated drug distribution map from scan 2 is provided to the model to predict the tumor at the time of scan 3. Therefore, the concentration of drug in the tumor tissue is spatially non-uniform and temporally varying based on the individual patient's response to therapy and NAT schedule.

All simulation codes and numerical calculations were written and executed in MATLAB (MathWorks, Natick, MA). The model was implemented in three dimensions (3D) using a fully explicit finite difference scheme with $\Delta t = 0.25$ day with the mesh dimensions defined by the size of the DCE-MRI voxels. The size of the computational domain is set by a rectangle whose dimensions are determined by the size of the breast for each patient. To reduce computation time for all calibrations, the voxel matrix within this designated rectangular domain was down sampled by a factor of two. A no flux boundary condition was prescribed at the boundary of the breast. To calibrate model parameters, a Levenberg–Marquardt (LM) least squares non-linear optimization

is used, where the sum of squared errors between the simulated tumor cell numbers from the model and the calculated tumor cell densities from the imaging data is minimized. See ref. [25] for additional details on the full development of these numerical methods.

Table S.2: Description of the variables of the model system including the assigned parameter values and specification of units.

Variable	Description	How assigned
$N_{TC}(\bar{x},t)$	Number of tumor cells in the voxel at position $\bar{x}$ at time t	Derived from the DW-MRI data
$D(\bar{x},t)$	Diffusion coefficient of tumor cells, where $D = D_0\exp(-\gamma\sigma_{vm}(\bar{x},t))$ (mm^2/day)	Coupled to the breast tissues
σ_{vm}	Von Mises stress (kPa)	Calculated
$\vec{u}(\bar{x},t)$	Displacement vector due to tumor cell growth (mm)	Calculated
G	Shear modulus due to breast tissue properties, where $G = E/(2(1-\nu))$ (kPa)	Calculated
$C_{tissue}^{drug}(\bar{x},t)$	Concentration of drug in the tissue in the voxel at position $\bar{x}$ at time t (μM)	Derived from the DCE-MRI data

Table S.3: Description of the parameters for the model system including the assigned values and specification of units.

Parameter	Description	How assigned
D_0	Diffusion coefficient of tumor cells without stress	Calibrated, mm^2/day
γ	Mechanical coupling coefficient for stress	Assigned at 2.0×10^{-3} (1/kPa)
ν	Poisson's ratio	Assigned, 0.45 (dimensionless)
E	Young's modulus for adipose, fibroglandular, and tumor tissues	Assigned, 4 kPa, 2kPa, and 20 kPa, respectively *[35]*
λ	Coupling constant for displacement of tumor cells	Assigned as 2.5×10^{-3} (dimensionless)
$k(\bar{x})$	Proliferation rate of tumor cells per voxel	Calibrated, 1/day
θ	Carrying capacity of tumor cells in the voxel at position $\bar{x}$	Calculated, 2.02×10^6 cells
α	Efficacy of the drug against tumor cells	Calibrated, 1/(μM·day)
β	Drug exponential decay rate	Calibrated, 1/day

Statistical analysis

To test the accuracy of the model's predictions, we generate a Monte Carlo estimated p value for testing the significance of the average absolute difference between the model's predictions and measured outcomes versus random sampling. This is a standard bootstrap random resampling approach, described in detail in ref. [1]. For our particular application, we test the null hypothesis that the mean difference is not equal to a delta value of 10%, 15%, or 20% error (determined using the established variation in the MRI measurements [2]) *via* the following steps:

1. Calculate the absolute difference between the model's prediction and measured tumor response for each patient (N = 18)
2. Calculate the average absolute difference for the cohort
3. Sample 500 times with replacement (sample size N = 18) the absolute differences of step 1
4. Calculate the average of each of the 500 samples constructed in step 3
5. Subtract the corresponding average delta from the average of each of the 500 samples
6. Calculate the proportion of times each delta adjusted sample average is less than the cohort average calculated in step 2.
7. Subtract the proportion calculated in step 6 from 1.0 to determine the Monte Carlo estimated p value.

We calculate this p values for each of the tumor response measures (i.e., total cellularity, volume, and longest axis).

Table S.4: Measured percent changes in total tumor cellularity, volume, and longest axis between scans. Highlighted patients were designated as "responders" by the RECIST criteria (CR or PR) applied to changes in longest dimension between scan 1 and scan 3.

	Tumor cellularity percent change		Tumor volume percent change		Longest axis percent change	
Patient	Scan 1 to Scan 2	Scan 1 to Scan 3	Scan 1 to Scan 2	Scan 1 to Scan 3	Scan 1 to Scan 2	Scan 1 to Scan 3
1	-	-	-	-	-	-
2	-3	-75	-2	-74	-2	-5
3	-31	-17	-25	-12	-8	-10
4	-33	-100	-37	-100	-14	-100
5	-15	-13	0	-18	23	7
6	11	-6	-1	-23	-14	-11
7	-	-	-	-	-	-
8	-31	-81	-32	-87	-12	-41
9	-52	-69	-47	-60	-16	-18
10	-27	-67	-21	-70	-25	-43
11	-66	-84	-65	-81	-22	-52
12	-73	-37	-74	-59	-34	32
13	44	21	-20	-24	-7	-13
14	-73	-86	-75	-86	-65	-63
15	-14	-62	-21	-63	-4	-22
16	-8	-	-5	-	-3	-
17	-43	-30	-47	-39	-44	-37
18	-39	-53	-40	-60	-24	-37
19	-24	-64	-21	-67	-10	-23
20	-4	-79	1	-78	23	-33
21	-52	-89	-40	-89	-12	-25
Median	-27	-65	-25	-65	-12	-24
Quartile Range	[-52, -4]	[-82, -26]	[-47, -5]	[-82, -36]	[-24,-4]	[-41,-11]

Supplemental references

1. Sorace, A.G., et al., *Repeatability, reproducibility, and accuracy of quantitative mri of the breast in the community radiology setting.* J Magn Reson Imaging, 2018.
2. Virostko, J., et al., *Magnetization Transfer MRI of Breast Cancer in the Community Setting: Reproducibility and Preliminary Results in Neoadjuvant Therapy.* Tomography, 2019. **5**(1): p. 44-52.
3. Li, X., et al., *Validation of an algorithm for the nonrigid registration of longitudinal breast MR images using realistic phantoms.* Med Phys, 2010. **37**(6): p. 2541-52.
4. Klein, S., et al., *elastix: a toolbox for intensity-based medical image registration.* IEEE Trans Med Imaging, 2010. **29**(1): p. 196-205.
5. Shamonin, D.P., et al., *Fast parallel image registration on CPU and GPU for diagnostic classification of Alzheimer's disease.* Front Neuroinform, 2013. **7**: p. 50.
6. Wu, C., et al., *Quantitative analysis of vascular properties derived from ultrafast DCE-MRI to discriminate malignant and benign breast tumors.* Magn Reson Med, 2018.
7. Yankeelov, T.E. and J.C. Gore, *Dynamic Contrast Enhanced Magnetic Resonance Imaging in Oncology: Theory, Data Acquisition, Analysis, and Examples.* Curr Med Imaging Rev, 2009. **3**(2): p. 91-107.
8. Li, X., et al., *A novel AIF tracking method and comparison of DCE-MRI parameters using individual and population-based AIFs in human breast cancer.* Phys Med Biol, 2011. **56**(17): p. 5753-69.
9. Jarrett, A.M., et al., *Incorporating drug delivery into an imaging-driven, mechanics-coupled reaction diffusion model for predicting the response of breast cancer to neoadjuvant chemotherapy: theory and preliminary clinical results.* Phys Med Biol, 2018. **63**(10): p. 105015.
10. Ohtsu, T., et al., *Clinical pharmacokinetics and pharmacodynamics of paclitaxel: A 3-hour infusion versus a 24-hour infusion.* Clinical Cancer Research, 1995. **1**(6): p. 599-606.
11. Juma, F.D., H.J. Rogers, and J.R. Trounce, *Pharmacokinetics of cyclophosphamide and alkylating activity in man after intravenous and oral administration.* Br J Clin Pharmacol, 1979. **8**(3): p. 209-17.
12. Green, R.F., et al., *Plasma Pharmacokinetics of Adriamycin and Adriamycinol: Implications for the Design of in Vitro Experiments and Treatment Protocols.* Cancer Research, 1983. **43**: p. 3417-3421.
13. Oguri, S., et al., *Clinical pharmacokinetics of carboplatin.* J Clin Pharmacol, 1988. **28**(3): p. 208-15.
14. Whisenant, J.G., et al., *Assessing reproducibility of diffusion-weighted magnetic resonance imaging studies in a murine model of HER2+ breast cancer.* Magn Reson Imaging, 2014. **32**(3): p. 245-9.
15. Weis, J.A., et al., *A mechanically coupled reaction-diffusion model for predicting the response of breast tumors to neoadjuvant chemotherapy.* Physics in Medicine and Biology, 2013. **58**(17): p. 5851-5866.
16. Weis, J.A., et al., *Predicting the Response of Breast Cancer to Neoadjuvant Therapy Using a Mechanically Coupled Reaction-Diffusion Model.* Cancer Research, 2015. **75**(22): p. 4697-4707.

17. Atuegwu, N.C., et al., *Parameterizing the Logistic Model of Tumor Growth by DW-MRI and DCE-MRI Data to Predict Treatment Response and Changes in Breast Cancer Cellularity during Neoadjuvant Chemotherapy.* Translational Oncology, 2013. **6**(3): p. 256-264.
18. Hagmann, P., et al., *Understanding diffusion MR imaging techniques: from scalar diffusion-weighted imaging to diffusion tensor imaging and beyond.* Radiographics, 2006. **26 Suppl 1**: p. S205-23.
19. Atuegwu, N.C., et al., *Integration of diffusion-weighted MRI data and a simple mathematical model to predict breast tumor cellularity during neoadjuvant chemotherapy.* Magn Reson Med, 2011. **66**(6): p. 1689-96.
20. Anderson, A.W., et al., *Effects of cell volume fraction changes on apparent diffusion in human cells.* Magn Reson Imaging, 2000. **18**(6): p. 689-95.
21. Martin, I., et al., *Computer-based technique for cell aggregation analysis and cell aggregation in in vitro chondrogenesis.* Cytometry, 1997. **28**(2): p. 141-6.
22. Weis, J.A., M.I. Miga, and T.E. Yankeelov, *Three-dimensional image-based mechanical modeling for predicting the response of breast cancer to neoadjuvant therapy.* Computer Methods in Applied Mechanics and Engineering, 2017. **314**: p. 494-512.
23. Hormuth, D.A., et al., *Predicting in vivo glioma growth with the reaction diffusion equation constrained by quantitative magnetic resonance imaging data.* Physical Biology, 2015. **12**(4).
24. Hormuth, D.A., et al., *A mechanically coupled reaction-diffusion model that incorporates intra-tumoural heterogeneity to predict in vivo glioma growth.* J R Soc Interface, 2017. **14**(128).
25. Hormuth, D.A., et al., *Mechanically Coupled Reaction-Diffusion Model to Predict Glioma Growth: Methodological Details.* Methods Mol Biol, 2018. **1711**: p. 225-241.
26. Hormuth, D.A., et al., *Mechanism-based Modeling of Tumor Growth and Treatment Response Constrained by Multiparametric Imaging Data.* Jco Clinical Cancer Informatics, 2019(3): p. 10.
27. Hormuth II, D., et al., *Predicting in vivo tumor growth and angiogenesis with an MRI calibrated biophysical model Neuro-Oncology*, 2017. **19**(suppl_6): p. vi23.
28. Hormuth II DA, et al., *Biophysical modeling of in vivo glioma response following whole brain radiotherapy in a murine model of brain cancer.* International Journal of Radiation Oncology • Biology • Physics 2018.
29. Barpe, D.R., D.D. Rosa, and P.E. Froehlich, *Pharmacokinetic evaluation of doxorubicin plasma levels in normal and overweight patients with breast cancer and simulation of dose adjustment by different indexes of body mass.* Eur J Pharm Sci, 2010. **41**(3-4): p. 458-63.
30. van der Vijgh, W.J., *Clinical pharmacokinetics of carboplatin.* Clin Pharmacokinet, 1991. **21**(4): p. 242-61.
31. Mori, T., et al., *Retention of paclitaxel in cancer cells for 1 week in vivo and in vitro.* Cancer Chemother Pharmacol, 2006. **58**(5): p. 665-72.
32. Tew, K., *Paclitaxel.* Reference Module in Biomedical Sciences, 2016.
33. Yang, L., et al., *Pharmacokinetics and safety of cyclophosphamide and docetaxel in a hemodialysis patient with early stage breast cancer: a case report.* BMC Cancer, 2015. **15**: p. 917.

34. Powis, G., et al., *Effect of body weight on the pharmacokinetics of cyclophosphamide in breast cancer patients.* Cancer Chemother Pharmacol, 1987. **20**(3): p. 219-22.
35. McKnight, A.L., et al., *MR elastography of breast cancer: preliminary results.* AJR Am J Roentgenol, 2002. **178**(6): p. 1411-7.